Deciphering Rapid Cell Signaling and Control of Cell Motility by Reverse Opto-Chemical Engineering

H. Hamzeh,[1,2,*] A. Gong,[1,*] M. Balbach,[1,2] D. Fridman,[1,2] H. G. Körschen,[1] R. Pascal,[1] F. Lavryk,[1] A. Rennhack,[1] R. Seifert,[1] A. Hernandez-Clavijo,[3] S. Pifferi,[3] V. Dusend,[4] B. K. Fleischmann,[4] P. Sasse,[4] A. Menini,[3] B. M. Friedrich,[5,6,†] L. Alvarez,[1,2,7,‡] and U. B. Kaupp[1,2,8,9,§]

[1]*Max Planck Institute for Neurobiology of Behavior–caesar, Molecular Sensory Systems, Ludwig-Erhard-Allee 2, 53175 Bonn, Germany*

[2]*Marine Biological Laboratory, 7 MBL Street, Woods Hole, Massachusetts 02543, USA*

[3]*SISSA, Neurobiology Group, via Bonomea 265, 34136 Trieste, Italy*

[4]*Institute for Physiology I, Medical Faculty, University of Bonn, Nussallee 11, 53115 Bonn, Germany*

[5]*Cluster of Excellence Physics of Life (PoL), Biological Dynamics and Self-organization Group, TU Dresden, Arnoldstr. 18, 01307 Dresden, Germany*

[6]*Center for Advancing Electronics Dresden (cfaed), Biological Algorithms Group, TU Dresden, Helmholtzstr. 18, 01069 Dresden, Germany*

[7]*Max Planck Institute for Neurobiology of Behavior–caesar, Neural Information Flow Group, Bonn 53175, Germany*

[8]*University of Bonn, Life & Medical Sciences Institute (LIMES), Carl-Troll-Str. 31, 53115 Bonn, Germany*

[9]*Max Planck Institute for Multidisciplinary Sciences, Biophysics of Cellular Signal Transduction, Am Fassberg 11, 37077 Göttingen, Germany*

(Received 18 March 2024; accepted 18 November 2025; published 13 February 2026)

Cells transform complex environmental stimuli into physiological responses. In dynamic environments, or when a motile cell moves in a static setting, stimuli change over time. Here we introduce a concept, "reverse opto-chemical engineering," which uses temporal light patterns and photo-triggers to create virtual sensory landscapes for cells. This allows us to record their physiological responses and motor behavior in real time. Using this approach, we studied cyclic-nucleotide signaling in sperm cells and mapped their stimulus-response transfer function. The technique can be employed for remote control of motility by light. Exploiting the chemotactic signaling backbone, we enable sperm to navigate in light gradients, making them attracted to light. This method offers possibilities for uncovering the mechanisms and signaling molecules behind rapid cellular computations, helping to understand the wiring diagram of cellular networks.

DOI: 10.1103/hlkj-7yxd

I. INTRODUCTION

Biological cells are exposed to numerous chemical and physical cues over multiple timescales that ultimately evoke a cellular response or control behavior. A key goal of biology is to understand the transfer function between stimulus input $s(t)$ and response output $o(t)$ in quantitative and molecular terms. This is challenging because cells face rich, spatially complex, and ever-changing chemical environments composed of puffs, plumes, ramps, periodic cycles, turbulences, or voids of diverse stimuli [1,2]. The complexity is further enhanced by feedback mechanisms that change the stimulus $s(t)$. For instance, stimulation of specific cells by a ligand may initiate down-regulation of ligand synthesis by other distant cell types. Another type of feedback comes from cell movements. As cells move, they sample a spatial distribution of sensory cues $c(\mathbf{r})$ along their path $\mathbf{r}(t)$. Movement translates the spatial information into a temporal stimulus $s(t) = c(\mathbf{r}(t))$; cells use this sensory information to continuously adjust their path [Figs. 1(a) and 1(b)]. This feedback, where movement determines future sensory input, is called 'information self-structuring' in engineering [3]. The main objective is to map in real time the biochemical circuits underlying navigation and behavioral feedback as cells move in a sensory landscape. However, emulating a naturalistic sensory landscape in the laboratory is experimentally challenging.

Consider chemotaxis, the directed movement of cells in a chemical gradient. Many organisms and cells are attracted by chemical factors that signal food, mates, or favorable conditions in general. Moving in periodic patterns like drifting circles, helices, or zigzag movements is an effective navigation strategy used by cells and animals to find a target [4–11]. Periodic locomotion patterns are also seen in other sensory behaviors like phototaxis [12,13] and during active exploratory whisking of rodents and marsupials [14]. The stimulus functions $s(t)$ generated by these movements are themselves periodic with frequencies that are typically $\geqslant$1 Hz.

A powerful approach for probing cellular signaling networks is to combine time-varying perturbations with signaling readouts from live cells [15–19]. This strategy was previously used to study slow cellular processes, like gene expression or filopodia outgrowth that proceed on a minute-to-hour timescale and, therefore, are experimentally accessible by intermittent stimulation and time-lapse recordings. However,

*These authors contributed equally to this work.
†Contact author: benjamin.m.friedrich@tu-dresden.de
‡Contact author: luis.alvarez@mpinb.mpg.de
§Contact author: benjamin.kaupp@mpinat.mpg.de

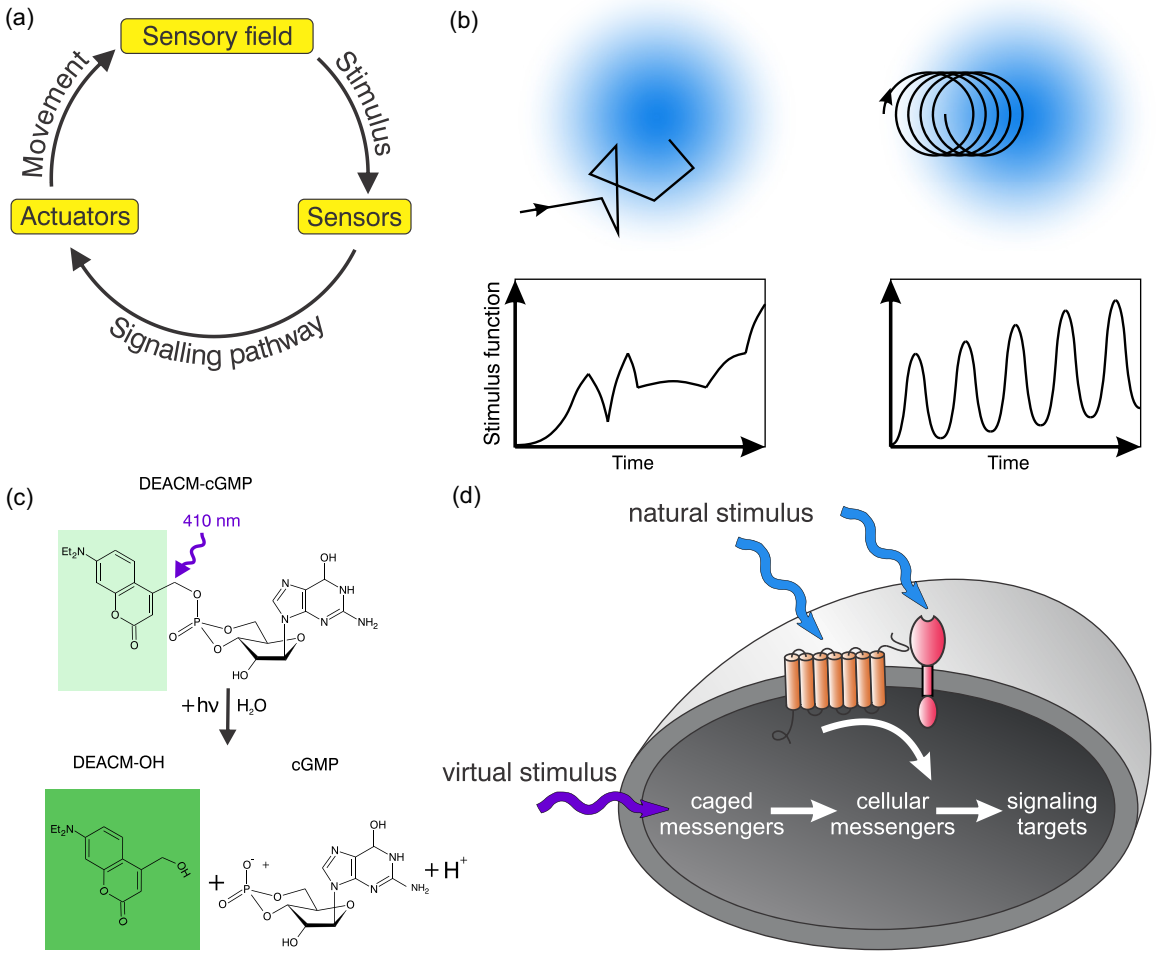

FIG. 1. Feedback loop between cell movement and stimulus from a sensory field. (a) The sensorimotor loop: cells gather information from their environment by cell sensors, and signaling pathways convert these stimuli into a motor response. As a cell moves through a sensory field, the registered stimulus function $s(t)$ changes dynamically, shaped by both the spatial sensory field and the cell's active movement in this field. (b) Examples of temporal stimuli (bottom) that result from two different paths across the same stimulus field (shades of light blue) (top). (c) Chemical structure of DEACM-caged cGMP. The caging group (light green) exhibits minimal background fluorescence. Exposure to a 410-nm light flash cleaves the covalent bond between the cage and cGMP. The fluorescence from the liberated DEACM-OH (dark green) enables quantification of messenger release. (d) Illustration depicts a cell responding to a natural stimulus (light blue arrows), which targets external receptors and initiates intracellular messenger production to regulate downstream signaling targets. By contrast, the opto-chemical engineering method bypasses these receptors by introducing a virtual stimulus (violet arrow) that releases messengers from caged precursors directly within the cell, effectively replicating natural signaling responses.

many biochemical signaling events happen in less than a second.

Here we extend this successful strategy to the millisecond time range using various waveforms of light and photo-triggers of the cellular messengers cAMP and cGMP [Fig. 1(c)]. This method allows creating a *virtual* stimulus input $s_v(t)$ [Fig. 1(d)] that mimics the stimulus encountered in natural sensory landscapes. The concept is reminiscent of reverse genetics, which introduces specific mutations into genes and analyzes the resulting phenotype; we term this approach accordingly reverse opto-chemical engineering (ROCE). While stimulating cells with time-varying light, we simultaneously record cellular responses using orthogonal potentiometric probes and Ca^{2+} indicator dyes. We study signaling events in sperm and present applications of this method to study cardiomyocytes and olfactory neurons.

This approach reveals the sensorimotor transfer function of sperm chemotaxis and demonstrates ROCE's versatility in understanding and manipulating cellular behavior. By emulating virtual sensory landscapes, we validated a theoretical model for sperm chemotaxis. Furthermore, we gained insights into sperm motility and revealed swimming behaviors resulting from a mismatch between sperm swimming and sensory perception. Using these insights, we precisely controlled sperm motility with light and "photoprinted" spatial patterns of sperm cells.

II. RESULTS

A. Implementation of reversed opto-chemical engineering

ROCE can be implemented through a virtual stimulus function, $s_v(t)$, using caged chemical compounds or op-

togenetic tools. While genetically encoded light-sensitive enzymes can be used for manipulating cyclic-nucleotide levels, such as photosensitive adenylate cyclase bPAC [20–22], rhodopsin/guanylate cyclase fusion proteins RhGC [23–25], and light-activated phosphodiesterases (LAPD) [26] are available, they have limitations for studying rapid signaling events: copy numbers and folding of proteins can vary and are often difficult to determine; the relationship between light energy and enzymatic activity tends to be complex or variable; activation and deactivation kinetics of the respective enzymes are typically too slow for probing millisecond-scale signaling [21,22]; and some light-sensitive enzymes, like bPAC and LAPD, exhibit basal activity that alters cellular resting states. Consequently, their use is less suitable for precise and quantitative analysis of subsecond signaling events.

Although optogenetic tools have been successfully employed to investigate slower cellular responses—such as chemotaxis of neutrophil-like HL60 cells [27]—these approaches present limitations for rapid and quantitative signal manipulation. To overcome such constraints for our specific aim, we opted for caged compounds—specifically DEACM-caged cyclic nucleotides (cNMPs)—to rapidly and precisely control cAMP and cGMP levels via light [28] [Fig. 1(c)]. DEACM-caged cNMPs remain completely inactive until irradiation and offer multiple advantages: (1) their high quantum yield (0.27) and activation spectrum ($\lambda_{\text{peak}} = 410\,\text{nm}$) [29] allows using low, nontoxic light intensities; (2) their ultrafast photochemistry ($\leqslant 10$ ns) [30] enables submillisecond triggering of physiological reactions; and (3) their spectral profile allows multiplexed fluorescence measurements of multiple cellular responses without interference, since UV light is not required for photorelease [31]. In contrast, some optogenetic tools, such as channelrhodopsin, often exhibit action spectra that overlap with the excitation spectra of common fluorescent reporters [32]. Yet there is no general application limit to optogenetic tools when spectral overlap is avoided and photocycle kinetics are sufficiently fast. Finally, photorelease of cNMP can be rigorously quantified and calibrated (see Sec. IV).

We tested ROCE using three types of waveforms $s_v(t)$: (1) a steplike increase, (2) a sinusoidal waveform, and (3) a steady linear ramp [Fig. 2(a)]. For stationary cells, these waveforms simulate a sudden change, rhythmic stimulation, and a continuous increase, respectively. The cumulative light-stimulated cAMP increase follows the integral

$$\text{cAMP}(t) = \int_0^t s_v(t)\mathrm{d}t, \tag{1}$$

where the virtual stimulus $s_v(t) = k_{\text{rel}}\, I(t)$ is determined by the product of the rate constant k_{rel} of photorelease and the intensity $I(t)$ of the photolyzing light. The fractional release of cAMP was quantified *in vitro* using enhanced fluorescence of the free DEACM-OH [30] [Fig. 2(a); see also Fig. S1(a), and Figs. S2(a)–S2(c) in the Supplemental Material (SM) [33]] and in CHO cells using the cADDis cAMP sensor (see Sec. IV) [Fig. 2(b); see also Fig. S1(b) and Figs. S2(d) and S2(e) [33]]. Experiments confirmed the theoretical prediction embodied in Eq. (1) *in vitro* and *in vivo* in cell populations and single cells: the three waveforms produced, respectively, linear, frequency-modulated linear, and quadratic rises of cAMP concentration *in vitro* and *in vivo* [Figs. 2(a) and 2(b)]. At longer stimulation times, the *in vivo* cADDis signal in populations of CHO cells leveled off [Fig. 2(b), middle panel] due to sensor saturation, as predicted by a simple binding model (see Sec. IV). After the light stimulus had been switched off, cADDis fluorescence remained elevated for several seconds, indicating negligible PDE activity in CHO cells on this timescale. Similar results were obtained by imaging cAMP levels in single cells [Fig. 2(c) and see Fig. S1(b) [33]]. In conclusion, the observed changes in cAMP closely match theoretical models. ROCE's applicability was also confirmed in cardiomyocytes and olfactory receptor neurons, which also use cyclic-nucleotide signaling (see Note 1 [33]).

Finally, to further explore ROCE's capabilities, we studied the sensory-motor loop of motile sperm while navigating virtual sensory landscapes.

B. Oscillations of sensory input and motor output are predicted to drive sperm chemotaxis

Sperm cells navigate up a concentration gradient of signaling molecules through chemotaxis, a process best characterized in marine invertebrates with external fertilization [34]. One influential theory, proposed by Friedrich and Jülicher, suggests a geometric mechanism of sperm chemotaxis [35,36]. Due to their asymmetric flagellar bending waves, sperm swim along circles when near surfaces [37–39]. In a chemoattractant gradient, these "circle swimmers" experience an oscillating concentration stimulus $s(t)$: as they follow their circular path, they repeatedly move up and down the chemical gradient during each swimming cycle, yielding a periodic variation in stimulus intensity at a frequency f_0 tied to their swimming motion.

The oscillatory stimulus $s(t)$ triggers oscillatory intracellular signaling events that modulate the asymmetry of the flagellar beat. As the beat asymmetry oscillates, so does the swimming path curvature $\kappa(t)$ [37]. When the path curvature oscillates around a mean value rather than remaining constant, a perfect circular swimming path (constant path curvature $\kappa(t) = \kappa_0$) transforms into a drifting circle (see Fig. S7 [33]).

A key feature of this theory is the phase shift ϕ between the oscillatory concentration stimulus and the oscillations in path curvature. This phase shift, a consequence of delays in biochemical signaling inside the flagellum, determines the direction in which the drifting circles move relative to the concentration gradient (see Fig. S8 [33]). In essence, the Friedrich and Jülicher [35] theory predicts that spatial concentration gradients are translated into temporal oscillations of three quantities: the stimulus, downstream signaling, and motor responses. These periodic signals guide sperm cells to navigate chemotactically along drifting circles. For further details on this theory, see Note 2 [33].

C. Applying ROCE to probe a theoretical model for sperm navigation

Next, we employ ROCE to study and manipulate chemotactic signaling and swimming behavior in sea urchin sperm, thereby providing a test for the Friedrich and Jülicher theory.

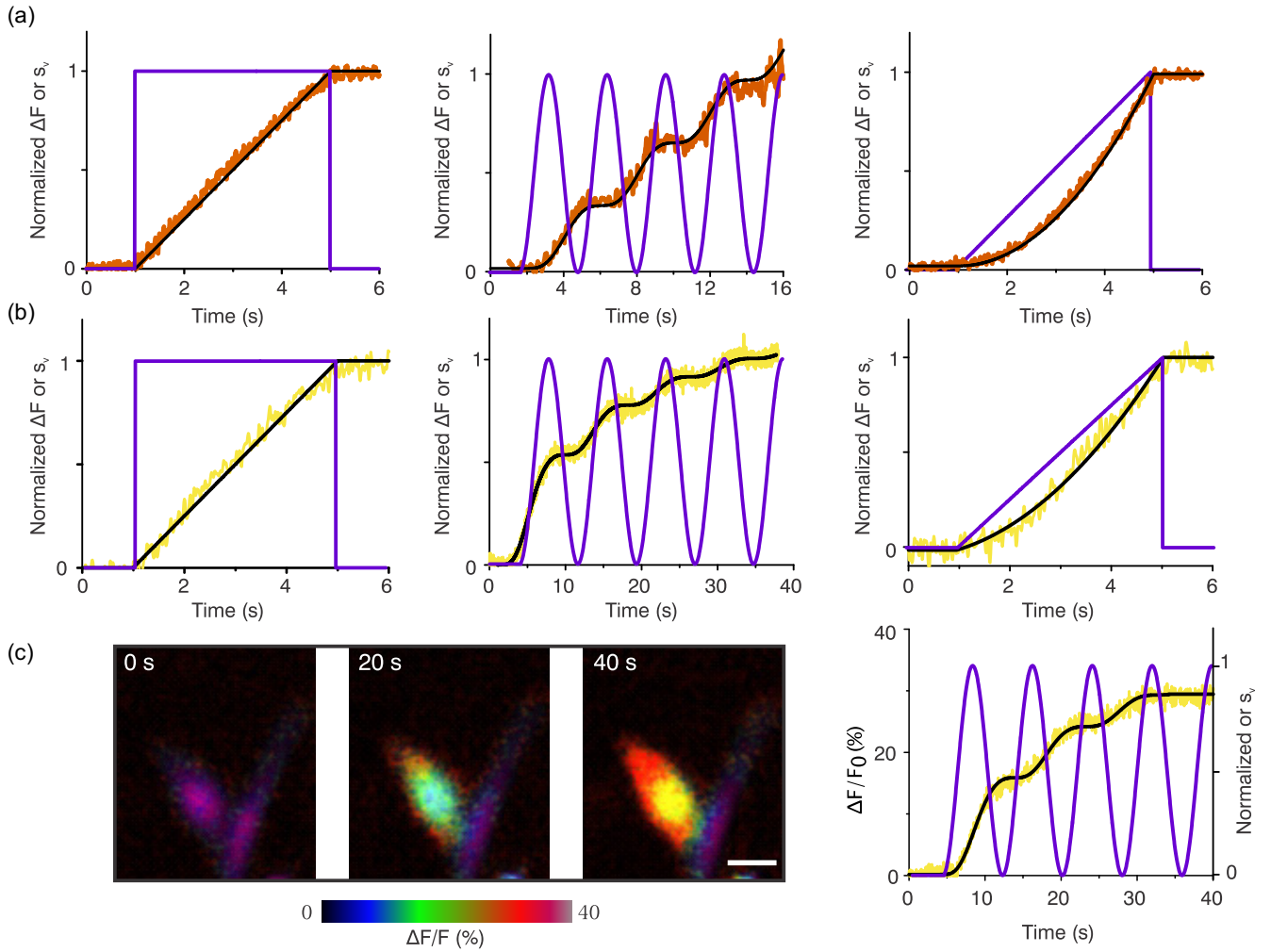

FIG. 2. Implementation of the ROCE method. (a) The time course of DEACM-OH fluorescence (orange) during photolysis by a virtual stimulus $s_v(t)$, with various stimulus waveforms shown (violet). The black traces represent the calculated cumulative cAMP release for each waveform. These data are from *in vitro* experiments using DEACM-caged cAMP (15 μM) in buffer ($\lambda_{exc} = 365$ nm; $\lambda_{em} = 490$ nm). (b) Fluorescence time course of the cAMP sensor cADDis (yellow) evoked by $s_v(t)$ in caged cAMP-loaded (15 μM) CHO cells; a black line shows a fit to a simple binding isotherm (see Sec. IV for details). (c) Single-cell imaging. Left: false-color images of cADDis-expressing HEK cells showing the fluorescence increase at three time points following periodic photorelease of cAMP by $s_v(t)$. Scale bar 20 μM. A color scale for the cADDis fluorescence intensity appears beneath the images. Right: fluorescence time trace (yellow) from a single cell. The black line shows a fit to a simple binding isotherm.

When swimming near surfaces, sperm cells trace chemoattractant gradients along drifting circles [36,40,41], generating self-entrained stimulus oscillations $s(t)$ at frequencies matching their circular swimming around 1 Hz. Chemoattractant binding to guanylyl cyclase receptors on the sperm flagellum initiates a signaling pathway (see Fig. S3 [33]), translating periodic stimulation into changes in $[Ca^{2+}]_i$, which in turn modulate the flagellar beat [40]. Within a timescale of 10 ms to 1 s, this signaling comprises a rapid rise of cGMP levels, a transient membrane hyperpolarization ΔV_m, and a rise of $[Ca^{2+}]_i$ [42]. To mimic $s(t)$ experienced by sperm swimming along drifting circles in a chemical gradient, caged cGMP-loaded sperm were exposed to oscillatory light patterns, while changes in $V_m(t)$ and $[Ca^{2+}]_i$ were recorded using fluorescent dyes [Figs. 3(a) and 3(b)].

The stopped-flow technique was used to examine the cellular responses of sperm populations following oscillatory cGMP release. These experiments provided several important insights. First, oscillatory virtual stimuli $s_v(t)$ evoked regular sinusoidal oscillations in $V_m(t)$ and $Ca^{2+}(t)$. Second, the frequency-modulated amplitudes of $V_m(t)$ and $Ca^{2+}(t)$ remained stable throughout stimulation, indicating that sperm responses, at least for physiological 1-Hz stimulation used here, do not adapt to oscillatory inputs $s_v(t)$ [Fig. 3(b)]. By contrast, a constant steplike increase in stimulating light produces a transient increase in $[Ca^{2+}]_i$ that would almost completely recover if recorded for sufficiently long time [Fig. 5(b) in Jikeli *et al.* [36]]. Third, at 1-Hz stimulation, the amplitude of the Ca^{2+} response increases linearly with release rates up to 10 nM s^{-1}, then saturates at a release rates of 100 nM s^{-1} (see Fig. S5 [33]). The linearity of the response for moderate stimulation will become important later for the characterization of stimulus-response relationship using transfer functions. Fourth, the $V_m(t)$ and $Ca^{2+}(t)$ oscillations were

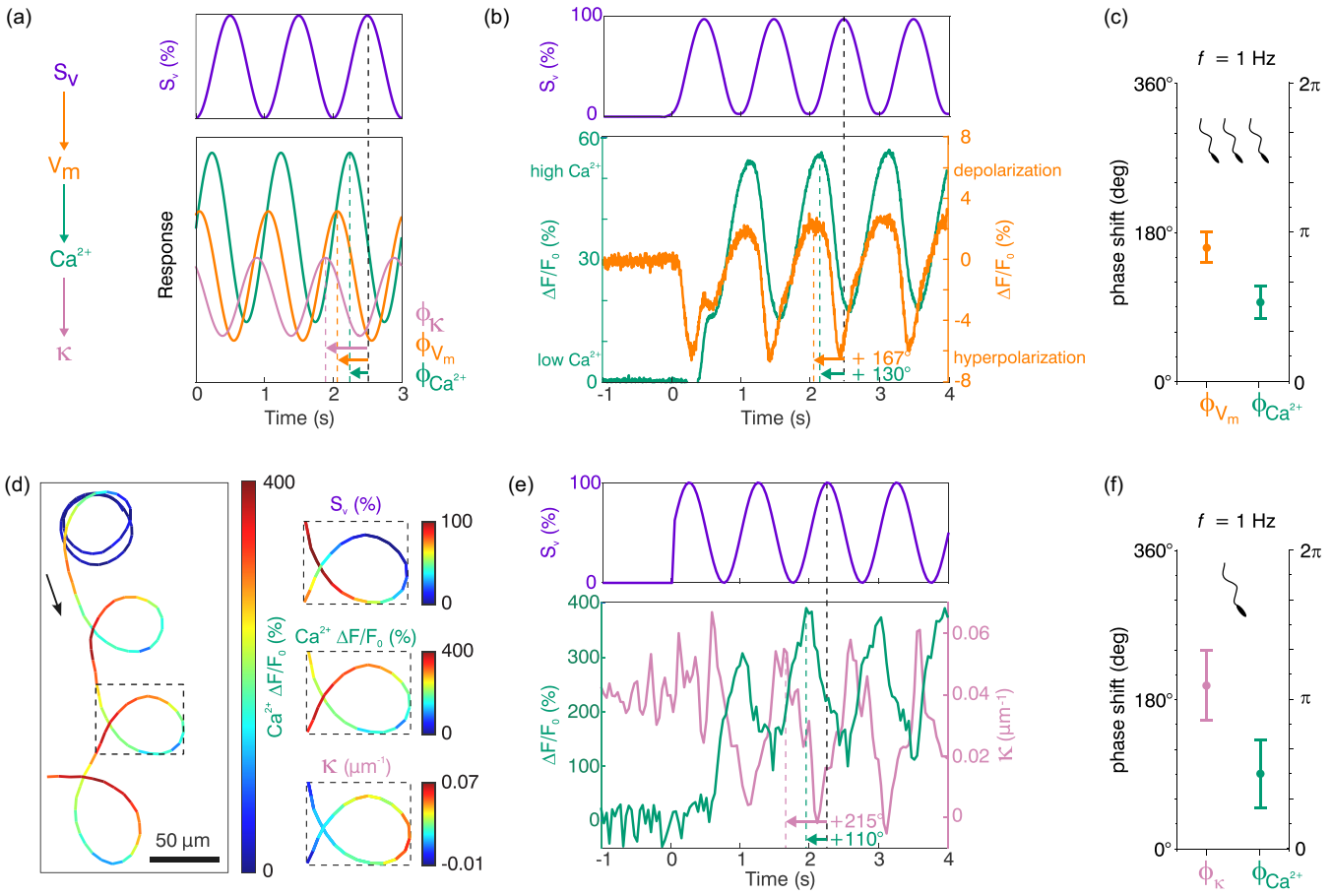

FIG. 3. Chemotactic signaling responses of sperm cells to oscillatory stimuli. (a) Schematic illustrating the experimental paradigm: An oscillatory virtual stimulus $s_v(t)$ is generated by releasing cGMP at a rate proportional to the intensity of an oscillatory light stimulus (violet), with cellular responses recorded sequentially. The sequence of events include the stimulus input, changes in membrane voltage V_m, intracellular Ca^{2+} concentration $[Ca^{2+}]_i$, and swimming path curvature κ, coded by color. (b) Changes in V_m (orange) and $[Ca^{2+}]_i$ (green) of sperm populations evoked by a 1-Hz sinusoidal virtual stimulus $s_v(t)$ (violet) were registered using the fluorescent potentiometric probe FluoVolt and the Ca^{2+} dye Fluo-4. The maximal light power for photolysis was 0.24 mW, corresponding to the release of 220 nM cGMP s^{-1}. (c) Interval plot shows measured phase shifts relative to the stimulus, including circular means and standard deviations for both V_m ($n = 4$) and Ca^{2+} ($n = 5$). (d) Swimming path of a sperm cell exposed to a 1-Hz virtual stimulus, showing the swimming direction (arrow) and color-coded Ca^{2+} signals along the path. Relative intensity of the light stimulus, Ca^{2+} signal, and path curvature are shown for the highlighted region (dashed box). (e) Time series plot presents the light protocol, evoked Ca^{2+} signal, and resulting path curvature (pink). (f) Interval plot summarizes measured phase shifts for path curvature κ and Ca^{2+} signal relative to the stimulus in single cells ($n = 4$).

phase-shifted with respect to oscillatory $s_v(t)$. The Ca^{2+} oscillations were phase-shifted by $\phi_{Ca} = 96.7° \pm 19.7°$ ($n = 5$), while the V_m oscillations were shifted by $\phi_{Vm} = 162.2° \pm 18.6°$ ($n = 4$) [Fig. 3(c)]. Standard sign conventions for phase shifts from physics were followed: for a sinusoidal stimulus defined as $\sin(2\pi f\, t)$, a corresponding response is described as $\sin(2\pi f\, t + \phi)$. Phase shifts reflect a latency of signaling. If the response is delayed by a latency time τ with respect to the stimulus, a phase shift of $\phi = 2\pi\,(1 - \tau/T)$ should be observed. For the Ca^{2+} response, the measured phase shift corresponds to an apparent latency of 730 ± 5 ms for 1-Hz stimulation, consistent with previous reports of kinetic measurements of Ca^{2+} responses [41–43]. For the V_m response, we need to take into account that an increase in stimulus causes a hyperpolarization, i.e., a decrease in V_m. Without latency, we would thus observe a phase shift of exactly π; with latency, we expect $\phi = 2\pi\,(1 - \tau/T) - \pi$. Thus, for the V_m response, the measured phase shift corresponds to an apparent latency of 50 ± 5 ms for 1-Hz stimulation, consistent with the almost instantaneous change in V_m [44].

The regular sinusoidal waveforms of $V_m(t)$ and $Ca^{2+}(t)$ responses indicate that sperm continuously sample their environment rather than continually probing gradients at discrete time intervals. This indicates that sperm convert a time-continuous analog input stimulus $s_v(t)$ directly into a time-continuous analog output response. Finally, $V_m(t)$ and $Ca^{2+}(t)$ signals are phase-locked with the oscillating virtual stimulus $s_v(t)$ [Fig. 3(b)].

Previous studies using repeated discrete stimulation (steps or brief pulses) showed that sperm integrate stimuli over a period of up to approximately 500 ms before responding [45]. Using the ROCE paradigm with continuous waveforms reveals that sperm integrate stimuli continuously and transduce into continuous responses.

D. Oscillatory stimuli and swimming behavior

We next examined how an oscillatory virtual stimulus influences swimming behavior. Specifically, we analyzed Ca^{2+} oscillations and changes in swimming paths in response to a 1-Hz oscillatory stimulus $s_v(t)$ applied to sperm loaded with caged cGMP [Figs. 3(d)–3(f); see Movie 1 [33]]. Video microscopy enabled precise tracking of sperm as they moved in 2D at the glass/water interface in a shallow recording chamber [Figs. 3(d)]. Before stimulation, sperm swam along regular circles characterized by a constant path curvature κ_0 [Figs. 3(d) and 3(e)]. When exposed to oscillatory light stimulation, both Ca^{2+} concentration and path curvature began to oscillate, causing sperm to swim along drifting circles [Figs. 3(d) and 3(e)]. The drift, reminiscent of sperm chemotactic navigation, can be explained theoretically (see Note 2 [33]) as arising from oscillations of path curvature κ at the frequency of circular swimming [35,40]. Critically, the phase shift between the stimulus and the path curvature determines the direction of drift.

Analysis of single-cell responses revealed phase shifts for $\kappa(t)$ of $\phi_\kappa = 197.0^\circ \pm 42.2^\circ$ and for $Ca^{2+}(t)$ of $\phi_{Ca} = 90.3^\circ \pm 41.2^\circ$ [$n = 4$; Fig. 3(f)]. Importantly, for positive chemotaxis, theory predicts that ϕ_κ should range between 180° and 360°. Thus, periodic light stimulation that triggers cGMP release successfully mimics the natural chemotactic 2D navigation pattern observed in a concentration gradient—even in the absence of an actual chemical gradient. These results reinforce the idea that the cGMP concentration in the flagellum oscillates during chemotactic navigation. In the ROCE experiment, cGMP oscillations are created through periodic photorelease of cGMP followed by hydrolysis via PDE activity (see Fig. 3 in Trötschel [44]). Under natural chemotaxis conditions, periodic stimulation and inactivation of GC lead to periodic cGMP synthesis, with subsequent removal of cGMP through PDE hydrolysis. Furthermore, shifting the phase of the stimulatory waveform, changes the direction in which the sperm's drifting swimming circles move (see Movie 2 [33]). Thus, core predictions of theory—periodic stimulation causes oscillations of signaling components such as cGMP, and drift direction is determined by phase shifts—are validated by these experimental findings [35].

E. Recording of transfer functions using ROCE

As a cell moves, the spatial concentration field, $c(\mathbf{r})$, is converted into a temporal stimulus, $s(t)$. When presented with an oscillatory input $s_v(t)$ at frequency f, the cellular outputs—$V_m(t)$, $Ca^{2+}(t)$, and path curvature $\kappa(t)$—each oscillate at the same frequency f around their respective steady-state levels [Figs. 3(b) and 3(e)]. Notably, the amplitude of these output oscillations scales linearly with that of the input oscillations, modulated by a proportionality factor $|\mathbf{H}(f)|$, which itself depends on the frequency f. Additionally, the output oscillations are phase-shifted relative to the input, with a phase shift $\phi = \arg \mathbf{H}(f)$ that also can vary with frequency f, as indicated by arrows in Fig. 3(a). Such input-output relationships can be described succinctly by a complex-valued transfer function $\mathbf{H}(f)$, also known as impedance or linear response function.

The transfer function $\mathbf{H}_{Ca}$ between input $s_v(t)$ and $Ca^{2+}(t)$ output was established using frequency sweeps from $f = 0.1$ to 10 Hz [Fig. 4(a) and Fig. S6 [33]]. The amplitude of the Ca^{2+} response was maximal at $f \leqslant 1$ Hz and declined at higher frequencies, yielding a cutoff frequency $f_c = 1.2 \pm 0.16$ Hz ($n = 4$) [Figs. 4(b) and 4(c) black]. Thus, the signaling network acts as a low-pass filter with a cutoff just below the 1-Hz frequency characteristic of circular swimming [36,40]. To validate the transfer function $\mathbf{H}_{Ca}$, a stimulus $s_v(t)$ representing the superposition of 1-Hz and 6-Hz oscillations was applied, revealing close agreement between the evoked Ca^{2+} signal and the response predicted by $\mathbf{H}_{Ca}$ [Fig. 4(d)].

Analogously, a stimulus-motor transfer function $\mathbf{H}_\kappa$ was defined to relate the stimulus $s_v(t)$ to changes in the path curvature κ: the motor response $\kappa(t)$ of swimming sperm [Figs. 4(b) and 4(c), pink]. Both $\mathbf{H}_\kappa$ for $\kappa(t)$ and $\mathbf{H}_{Ca}$ for $Ca^{2+}(t)$ exhibited similar cutoff frequencies [Fig. 4(b)]. Notably, the phase shift between these two transfer functions differed by approximately $\pi/2$ or 90° [Fig. 4(c)], aligning with previous findings that curvature is proportional to the time derivative of $[Ca^{2+}]_i$ [40]. Finally, phase shifts between $s_v(t)$ and both $Ca^{2+}(t)$ and $\kappa(t)$ decreased at higher frequencies, consistent with temporal averaging of the input stimulus.

To study sperm responses to periodic changes in chemoattractant concentration, a virtual chemical landscape was constructed. We calculated the temporal stimulus encountered by a sperm cell as it navigated along drifting circles in a spatial Gaussian chemoattractant profile, simulating swimming both up and down the concentration gradient [Figs. 4(e) and 4(f)]. This temporal pattern was then applied to a sperm population in a cuvette using a stopped-flow device. Both V_m and $[Ca^{2+}]$ displayed a characteristic waxing-and-waning pattern of oscillations during virtual swimming along both gradient directions [Fig. 4(g)]. At the peak of the light profile—aligning with the highest point of the Gaussian gradient—the amplitudes of V_m and Ca^{2+} oscillations approached zero [Fig. 4(g)]. This distinctive waxing-and-waning response is consistent with predictions from the transfer function $\mathbf{H}_{Ca}$ [Fig. 4(h)].

Two key insights emerge from this virtual-landscape experiment. First, sperm retain their responsiveness to periodic stimulation over a broad range of average stimulus strengths. Second, phase locking between the stimulus $s_v(t)$ and the responses $V_m(t)$ and $Ca^{2+}(t)$ is maintained regardless of whether sperm swim up- or down-gradient, preserving the typical response required for positive chemotaxis, even for a virtual stimulus corresponding to hypothetical conditions. We noted, however, when the stimulus declines toward zero, measured Ca^{2+} signals were larger than predicted. This discrepancy reveals nonlinearities during substantial stimulus drops, potentially induced by off-responses triggered during persistent down-gradient swimming [36,46]

F. Optical control of cell motility

To gain deeper insight into stimulus-motor coupling during physiological stimulation, experiments were conducted with 1-Hz sinusoidal stimuli. Sperm swimming along circular paths naturally sample concentration gradients precisely at the same frequency f_0 as their circular motion.

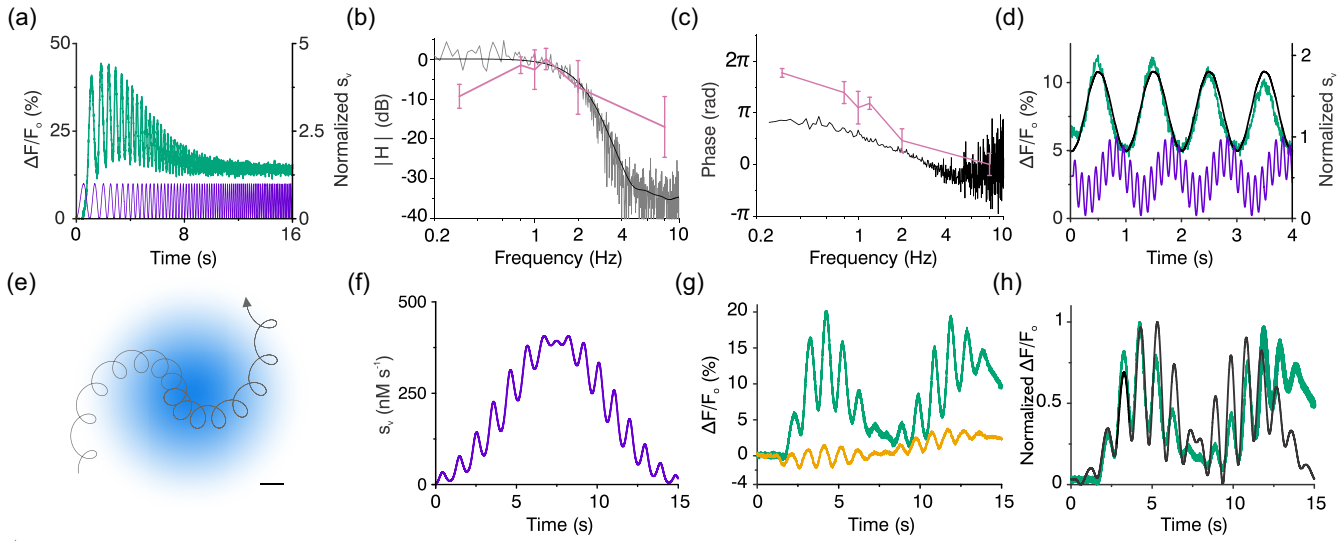

FIG. 4. The transfer functions of chemotactic signaling. (a) Frequency-dependent Ca^{2+} response (green) of sperm using a stimulus sweep $s_v(t)$ (violet) allowing determination of the signaling pathway's transfer function. $\Delta F/F_0$ indicates changes in $[Ca^{2+}]_i$. (b) Estimated magnitude of the raw (gray) and smoothed (black) transfer function $|\mathbf{H}(f)|$ of the Ca^{2+} response and of the curvature amplitude ±s.d. (pink). (c) Phase relation between Ca^{2+} signal and stimulus (black) and path curvature and stimulus (pink) as a function of stimulus frequency. (d) Validation of the transfer function using a composite $s_v(t)$, a superposition of two sinusoidal oscillations at 1 Hz and 6 Hz (violet); the Ca^{2+} signal (green) is compared with the predicted output signal (black) generated by applying the transfer function to the input signal. (e) Schematic of emulating chemotactic signaling in a virtual gradient, depicting a hypothetical swimming path (light gray) through a Gaussian-shaped concentration profile (blue gradient). The swimming direction is marked by an arrow (scale bar 100 μM). (f) The corresponding virtual stimulus function $s_v(t)$ that replicates the sensory stimulus a sperm cell would encounter when traversing this concentration field along the hypothetical path. (g) Changes in voltage V_m (orange) and $[Ca^{2+}]_i$ (green) during navigation in the virtual concentration field were monitored using the FluoVolt and Fluo-4 dyes, respectively. (h) The output Ca^{2+} signal (black), predicted by convolution of $s_v(t)$ with the transfer function $\mathbf{H}_{Ca}$ from (b) and (c), aligned with the actual measured Ca^{2+} signal (green).

Theoretical models predict that, during chemotaxis, oscillations in path curvature cause sperm to swim on drifting circles [35]. Experiments confirm this prediction: when subjected to an oscillatory stimulus $s_v(t)$ matching the circular swimming frequency f_0, sperm indeed swim on drifting circles [40,47]. However, what happens when the stimulus frequency deviates from the natural swimming frequency?

To explore this question, the ROCE approach was used to disrupt the natural synchronization (self-entrainment) between the stimulus frequency f_s and the frequency f_0 of circular swimming. The behavior of sperm loaded with caged cGMP was observed in shallow recording chambers. Under these conditions, the circular swimming frequency f_0 was approximately 1 Hz but varied slightly between individual sperm cells [36,40]. We exploited this natural variability to probe the case where f_s and f_0 differ. When presented with a virtual stimulus oscillating precisely at 1 Hz, the sperm swimming paths resembled intricate "spirograph orbits"—complex, multilobed trajectories reminiscent of patterns produced by a Spirograph toy [Fig. 5(a); see also Movie 3 and Table SI [33]]. These multilobed trajectories, known as epicycloids in mathematics, arise from a pen attached to a gear rotating inside a larger circle [Fig. 5(a) and Fig. S9 [33]]. The numbers and position of lobes varied: high-curvature "lobes" appeared inside the centerline of the super-circular path for $f_s < f_0$ and outside for $f_s > f_0$ [see Figs. S9(b) and S9(c) [33]].

An extension of the theory framework by Friedrich and Jülicher [35] predicts such epicycloid swimming trajectories when the stimulus frequency f_s deviates from the cell's natural circular swimming frequency f_0 [Fig. 5(b); see Note 3 [33]]. The underlying principle is intuitive: if f_s matches f_0 perfectly ($f_s = f_0$), the velocity vector $\mathbf{v}$ of the cell retains the same direction before and after each complete cycle of stimulus oscillations, resulting in swimming circles that drift along straight lines [Fig. 5(b); see also Fig. S9(a) [33]]. Thus, for self-entrained oscillations ($f_s = f_0$), sperm follow drifting circles featuring almost straight centerlines. If f_s and f_0 differ, however, $\mathbf{v}$ undergoes a nonzero net rotation after each stimulus cycle. This causes swimming cells to move on epicycloid paths—essentially, drifting circles whose curved centerline itself forms a circle [Fig. 5(b); see also Figs. S9(b) and S9(c) [33]]. The frequency with which the cell orbits this circular centerline equals the frequency difference $|f_s - f_0|$, producing spirograph-like trajectories with $n = f_s/|f_s - f_0|$ lobes. The diversity of observed swimming paths (see Table I [33]) is thus fully accounted for by variations in the intrinsic frequency f_0 (arising from variations in swimming velocity, circle diameter, or both), demonstrating good agreement between experimental observations and theoretical predictions.

These experiments reveal a fundamental insight: effective sperm navigation requires the frequency of the external oscillatory stimulus to match that of their intrinsic swimming motion. When sperm traverse a concentration gradient, this motility-stimulus synchronization naturally occurs, optimizing their chemotactic behavior [Fig. 1(a)].

The findings suggest it is possible to remotely guide sperm by delivering a virtual stimulus that synchronizes with their swimming frequency. While this could be achieved through

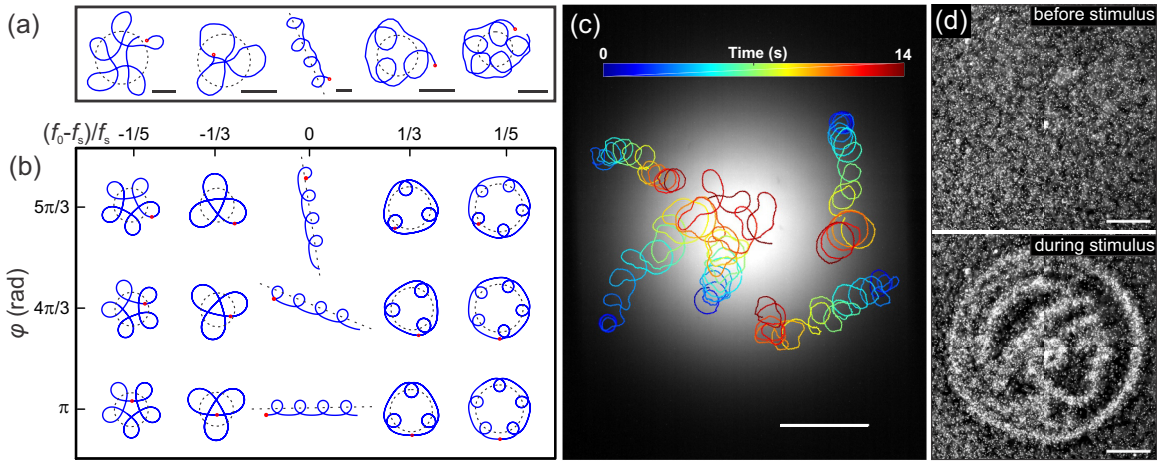

FIG. 5. Control of sperm motility by light. (a) Collection of experimental trajectories of caged cGMP-loaded sperm exposed to a 1-Hz sinusoidal UV-light stimulus. Each trajectory starts from a red dot; the centerline of trajectories is shown as dashed black lines. Scale bars 50 μM. (b) Predicted swimming trajectories for cells with path curvature $\kappa(t)$ oscillating at the stimulation frequency f_s and exhibiting a phase shift ϕ relative to the stimulus $s_v(t)$. Rational ratios of the circular swimming frequency f_0 to f_s determine the n-fold symmetry of trajectories (columns). Different values of ϕ generate the same geometric forms, rotated in space (rows) (see Note 3 in the SM [33]). (c) Swimming paths of sperm ascending a Gaussian-shaped profile of light intensity in the absence of chemoattractant. While traversing the light profile, cGMP is released according to the local stimulus light intensity (gray shades); color code indicates time; scale bar 200 μM. (d) Light stimulation allows precise remote control of sperm movement, with cells being guided to form a Minerva silhouette. Each white dot corresponds to a single sperm cell visualized by dark-field microscopy. Images show conditions before (top) and 5 s after the stimulus light is switched on (bottom). Scale bars 500 μM.

a closed-loop system that tracks sperm in real time, adjusting stimulus frequency (e.g., light intensity) dynamically, a simpler solution is to use a static gradient of light intensity. In such a light gradient, intracellular cGMP oscillates at the same frequency as circular swimming motion, activating the downstream signaling cascade that produces an oscillatory motility response. ROCE should enable precise directional control of motile cells by harnessing gradients of light intensity, effectively "hijacking" the chemotactic signaling pathway. As a proof of concept, sperm were successfully reprogrammed from chemotactic (attracted by chemicals) to "phototactic" (attracted by light) behavior. When exposed to a Gaussian profile of light intensity, sperm navigated up the gradient [Fig. 5(c); see also Movie 4 [33]]. Furthermore, by applying specific light patterns, we demonstrate the ability to "paint" images using cell-density distributions [Fig. 5(d); see also Movie 5 [33]].

III. DISCUSSION

We introduce a method, ROCE, to investigate motile cell behavior by exposing cells to a time-varying virtual stimulus $s_v(t)$ while simultaneously recording their biochemical, electrical, and behavioral responses. This quantitative approach allows precise analysis of physiological responses on a millisecond timescale. Although ROCE was demonstrated for the ubiquitous messengers cAMP and cGMP, the method should be broadly adaptable to other chemical photo-triggers, including caged forms of Ca^{2+}, phosphoinositides, lipids, proteins, gases like CO_2 [48], or optogenetic enzymes coupled to suitable sensors. Using multiple photo-triggers, ROCE enables investigation of the interplay between various signaling pathways.

To illustrate its capabilities, we applied ROCE to sperm chemotaxis. ROCE offers several key insights. First, oscillating $s_v(t)$ generates corresponding oscillatory voltage responses in sperm. Because the CNGK channel responsible for generating an electrical signal does not inactivate or desensitize at high cGMP concentrations [49], periodic stimulation reliably produces phase-locked oscillations of cGMP concentration, likely maintained by a dynamic balance between cGMP synthesis and hydrolysis. Second, sperm continuously sample stimuli in real time rather than "sniffing" at intervals, with almost instantaneous responses to stimulus changes. Third, the signaling pathway acts as a low-pass filter, attenuating high-frequency stimulus fluctuations above 1 Hz. Such high-frequency fluctuations may stem from micro-inhomogeneities of chemoattractant distribution, spontaneous fluctuations of flagellar motion [50], or shot-noise in chemosensation at low chemoattractant concentrations [46]. Fourth, the swimming paths are indistinguishable whether propelled by self-entrained oscillations or virtual stimulus oscillations matching the natural swimming frequency ($f_s = f_0$).

ROCE opens possibilities for simulating realistic sensory environments, such as chemical concentration fields shaped by fluid flow. This includes scenarios like metabolite delivery in the bloodstream or fluid transport by motile cilia in tissues such as the olfactory epithelium or brain ventricles [51,52]. Another promising application is the study of chemotactic behavior in slowly moving cells subjected to repetitive wave fronts of chemoattractant, such as those seen in the slime mold *Dictyostelium discoideum.* These cells respond to the initial rise in chemoattractant concentration as a wave reaches them. However, their behavior during the subsequent decline phase—once the wave has passed—remains an open debate

in current research, commonly referred to as the "back-of-the-wave" problem [53,54]. Studies using microfluidic techniques have produced contrasting findings: while one group reported that *D. discoideum* cells continue to migrate [53], another group reported that cells stop or even reverse their migration direction [55]. Approaches such as ROCE may provide fresh perspectives on this phenomenon by enabling investigation from alternative methodological angles.

Chemotactic gradient sensing relies on two main strategies: *spatial* comparison and *temporal* comparison [56–59]. Spatial comparison involves detecting a stimulus gradient across the cell's diameter, while temporal comparison is based on perceiving changes in stimulus strength over time as the cell moves through the environment.

ROCE provides a powerful tool for distinguishing between spatial and temporal mechanisms of gradient sensing. By applying a temporally varying but spatially uniform virtual stimulus, researchers can selectively activate cells that rely on temporal comparison, while those cells that depend on spatial comparison remain unaffected. Additionally, ROCE enables investigation of additional sensory behaviors such as thermotaxis, magnetotaxis, and phototaxis by targeting the relevant cellular messengers.

We propose that ROCE can be leveraged to unravel cellular computations at various points along signaling pathways, employing realistic virtual stimuli that clarify how cells process information and make decisions in complex environments.

Finally, it has been proposed that diverse sensory systems, from sperm chemotaxis to algae phototaxis, may operate according to common principles of sensory-motor coupling [60–62]. ROCE supports this concept by enabling the reprogramming of sperm cells from chemotactic to phototactic behavior, highlighting its versatility for studying and manipulating cellular responses across different sensory modalities.

IV. METHODS

A. Stopped-flow measurements using the lock-in detection principle

Changes in $[Ca^{2+}]_i$, and voltage V_m were measured using a rapid-mixing device (SFM-400; BioLogic) operated in stopped-flow mode at 18 °C [42] (see Fig. S1 [33]). The changes in $[Ca^{2+}]_i$, and V_m were measured with the Ca^{2+} indicator Fluo-4-AM and the voltage-sensitive indicator FluoVolt (Molecular Probes), respectively. For loading, dry sperm were suspended 1:6 (v/v) in loading buffer containing artificial seawater (ASW), the specific indicator dye (10 μM) and 0.5% Pluronic F127 (Sigma-Aldrich or Molecular Probes). Sperm were incubated for 30–60 min (Fluo-4-AM) or 15-30 min (FluoVolt) at 18 °C (for details see [42]). After incubation, the sample was diluted 1:20 with ASW containing DEACM-caged cGMP (15 μM, if not otherwise indicated) and 0.25% (w/v) Pluronic F127. The caged cGMP was allowed to equilibrate across sperm membranes for 7 min, and equilibration was checked by applying light flashes to photorelease cGMP and evoke a V_m or Ca^{2+} response. The amplitude of V_m responses plateaued after 7 min and stayed stable for up to 20 min. Throughout each experiment (about 15 min), sperm were maintained in ASW containing caged cGMP to prevent leakage after dilution. For recording, the sperm suspension (about 3×10^8 cells/ml) was rapidly mixed 1:1 (v/v) at a flow rate of 1 ml/s with ASW in the stopped-flow device. Leakage of caged cGMP after 1:1 mixing was negligible during recordings up to 30 s.

Fluorescence of indicators was excited using a SpectraX Light Engine (Lumencor). The excitation light was modulated at a reference frequency of 10 kHz and delivered to the cuvette via a liquid light guide. Emitted fluorescence was recorded by photomultiplier modules (H9656-20; Hamamatsu Photonics) and processed with digital lock-in amplifiers (Model 7230, Signal Recovery, Oakridge, TN, USA), which enhance the signal-to-noise at the reference frequency while excluding unrelated noise and signals at different frequencies. This detection setup enabled simultaneous photorelease of the caged compounds and fluorescence measurement with the amplifiers recovering only fluorescence modulated at 10 kHz, effectively filtering out fluorescence from uncaging events. Data were acquired using an acquisition pad (PCI-6221; National Instruments) and Bio-Kine software (BioLogic). Fluo-4 fluorescence was excited by a cyan LED (band-pass filter ET 490/20; Chroma), and emission was recorded after a band-pass filter (BrightLine 536/40; Semrock). For the FluoVolt dye, excitation was by a teal LED (band-pass BrightLine 513/17; Semrock), and emission was collected using a band-pass filter (BrightLine 542/20; Semrock). Signals represent the average of at least two recordings and are depicted as percent changes in fluorescence (ΔF) relative to the mean baseline (F_0), determined from the first 5–10 data points before the onset of the signal. The control (ASW) $\Delta F/F_0$ signals were subtracted from those induced by resact or cGMP, isolating the specific response.

B. Experimental determination of photorelease

The experimental estimation was based on the property that the DEACM cage exhibits minimal fluorescence when attached to cNMP, but becomes highly fluorescent after release by photolysis [see Fig. S2(a) [33]] [30]. The increase in fluorescence was measured by UV excitation at progressively higher light intensities, and the resulting fluorescence curves were normalized to each corresponding light level. The change in fluorescence over time was fitted with an exponential function [see Fig. S2(a) [33]]:

$$F(t) = F_0 + A[1 - e^{-k_{rel}t}], \tag{2}$$

where $F(t)$ denotes fluorescence at time t, F_0 represents background fluorescence, A is a constant, and k_{rel} is the release rate. The slope of the curve versus power density provided a linear fit consistent with theoretical predictions [see Fig. S2(b) [33]] and was subsequently used to estimate photorelease for various waveforms.

C. Theoretical estimate of photorelease

The release efficiency of caged compounds can be derived analytically using the Beer-Lambert law. The attenuation of light as it passes through a solution containing caged compounds at a concentration c is given by

$$E_t/E_i = 10^{-\varepsilon(\lambda)cl}, \tag{3}$$

where $\varepsilon(\lambda)$ is the extinction coefficient at wavelength λ, l is the path length, E_i is the incident light energy, and E_t is the transmitted light energy. For a typical $\varepsilon(\lambda)$ of $10\,000\,\mathrm{M}^{-1}\,\mathrm{cm}^{-1}$ [48], a caged compound concentration of $c \sim 10\,\mu\mathrm{M}$, and $l \sim 0.1\,\mathrm{cm}$, the exponent is $\sim 0.01 \ll 1$), enabling linearization by a Taylor expansion:

$$E_t/E_i \approx 1 - \varepsilon(\lambda) c l \ \ln\ 10. \tag{4}$$

Using the Planck-Einstein relation and Eq. (4), the number of absorbed photons n_a for a given wavelength λ can be estimated as

$$n_a(\lambda) = \frac{E_i \lambda \varepsilon(\lambda) c l \ \ln\ 10}{h c_{\mathrm{light}}}, \tag{5}$$

where c_{light} is the speed of light, and h is the Planck constant. The fraction of photons that lead to photolysis, n_r, is given by the quantum yield of photolysis ϕ, so the number of released molecules is $n_r = \phi n_a$. Considering the spectral flux of the light source $P(\lambda)$ and the flash duration t, for a narrow spectral band $\mathrm{d}\lambda$, the released molecules n_r are

$$n_r(\lambda) = \phi \frac{t P(\lambda) V \varepsilon(\lambda) c \ln 10}{h c_{\mathrm{light}}} d\lambda, \tag{6}$$

where V is the irradiated volume. The number of caged molecules before the flash in that volume is $n_o = V c N_{\mathrm{A}}$, where N_{A} is the Avogadro number. Integrating for all wavelengths, the fraction of released molecules per unit of time is

$$k_{\mathrm{rel}} = n_r/t n_o = \frac{\phi \ln(10)}{N_{\mathrm{A}} h c_{\mathrm{light}}} \int P(\lambda) \varepsilon(\lambda) \mathrm{d}\lambda. \tag{7}$$

The release from caged compounds by photolysis can be modeled as a first-order reaction of the caged compound with a photon:

$$c + \mathrm{h}\nu \xrightarrow{k_{\mathrm{rel}}} r, \tag{8}$$

where the concentration of the released compound is r. According to the mass balance equation and the principle of mass conservation:

$$\frac{\mathrm{d}r}{\mathrm{d}t} = k_{\mathrm{rel}}(c_0 - r), \tag{9}$$

where c_o is the caged compound concentration before photolysis. The solution for this equation is, assuming k_{rel} is constant:

$$r = c_o(1 - e^{-k_{\mathrm{rel}} t}). \tag{10}$$

Combining Eqs. (7) and (10), the total release can be quantified:

$$r = c_o\Big(1 - e^{-\frac{\phi t \ln 10}{N_{\mathrm{A}} h c_{\mathrm{light}}} \int_0^{\lambda} P(\lambda)\varepsilon(\lambda)\cdot \mathrm{d}\lambda}\Big). \tag{11}$$

If the spectral flux of the light source varies with time ($P = P(t,\lambda)$), a more general solution to Eq. (9) involves integrating the following expression over both time and wavelength, allowing for accurate predictions under complex illumination protocols:

$$r = c_o\Big(1 - e^{-\frac{\phi \ln 10}{N_{\mathrm{A}} h c_{\mathrm{light}}} \int_0^{\lambda} \int_0^{t} P(\lambda,t)\mathrm{d}t\, \varepsilon(\lambda)\mathrm{d}\lambda}\Big). \tag{12}$$

For users, a graphical user interface written in Python is available for evaluating the release of several compounds with different light sources and illumination protocols [63].

D. Calibration of intracellular caged cNMP concentrations and fractional cNMP release

Calibration of ROCE for precise quantification of cell signaling was achieved by determining both intracellular caged-cNMP concentrations and fractional photolysis using experimental and theoretical methods; both approaches agree within 30% (see Fig. S2 [33]).

Neutral DEACM-caged cNMPs readily equilibrate across cell membranes and, unlike acetomethoxy esters, should not accumulate within cells. Consequently, extra- and intracellular cNMP concentrations should be approximately equal. We tested this premise in two different cell systems by distinct methods. First, sperm were loaded with 1–25 μM DEACM-caged cGMP. The photolytic cGMP release for the different concentrations was kept constant by adjusting light energy accordingly. Sperm respond to stimulation by chemoattractant or cGMP with a hyperpolarization of membrane potential V_m [64]. The cGMP-evoked V_m responses perfectly superimposed [see Fig. S2(c) [33]], demonstrating that external and cytosolic caged compound concentrations scale linearly or are equal.

Second, we determined the K_{D} constant of cAMP binding to a cAMP sensor, named the cAMP Difference Detector *in situ* (cADDis) [65], in CHO cells via light titration [see Figs. S2(d) and S2(e) [33]]. The cADDis sensor is a fusion between a fluorescent reporter protein and the guanine-exchange factor regulated by cAMP, EPAC2, which includes two cyclic-nucleotide binding domains (CNBDs) with different affinities for cAMP [66]; only one CNBD is required for the conformational change [67]. Various versions of the cADDis sensor exist (see, for instance, [65]). The cADDis sensor used in this study contains only the CNBD of higher affinity, also referred to as the B-site (Red Fluorescent cAMP assay, Montana Molecular). Viral transduction of the cAMP sensor was performed according to the manufacturer's protocol.

Calibration of cADDis followed two distinct procedures. In the first procedure, 4×10^6 cells from a stable cell line expressing mlCNBD-FRET (another cAMP biosensor [68]), were mixed with cADDis BacMam stock, complete medium, and sodium butyrate, then plated on a 9-cm cell culture dish. Cells were incubated for 30 min at room temperature in the dark, then for 48 h at 37 °C and 5% CO_2. After incubation, cells were suspended in 500 μl hypotonic medium containing (in mM): 10 mM Hepes/NaOH) at pH 7.4 and 2 mM EDTA, and lysed by brief sonication three times for 10 sec. After centrifugation (500×*g*, 10 min), the supernatant was resuspended in 5 ml solution containing (in mM): NaCl 140, KCl 5.4, $MgCl_2$ 1, $CaCl_2$ 1.8, glucose 10, and Hepes 5 adjusted to pH 7.4 with NaOH. We recorded the fluorescence emission spectrum of cADDis (565–650 nm) excited at 550 nm. The cAMP was added stepwise, and spectra were again recorded. As a reference, we recorded from the same sample for each cAMP concentration the emission spectrum (460–580 nm) of mlCNBD-FRET, excited at 430 nm. Fluorescence values were plotted vs cAMP concentration and analyzed using a simple binding model. The K_{D} value for cAMP binding to cADDis and mlCNBD-FRET was 723.3 ± 45.1 nM ($n = 3$) and 144.7 ± 15.0 nM ($n = 3$), respectively. In the second procedure, cADDis was calibrated *in situ* by defined photolytic release of cAMP from caged cAMP-loaded CHO cells. The

changes in cADDis fluorescence were fit with a simple binding model using Origin (OriginLab), producing a K_D value of 628.3 nM, consistent with the first method (723.3 nM). These experiments demonstrate that photorelease of cNMP inside live cells allows for accurate, quantitative determination of intracellular cAMP levels.

E. cADDis imaging

HEK cells expressing cADDis, loaded with DEACM-caged cGMP (15 μM), were bathed in ES containing 0.01% Pluronic F127 (Sigma-Aldrich) and imaged in a custom-made observation chamber. Cyclic cAMP was released by a 365-nm UV LED (M365L2; Thorlabs) controlled by a custom-made power supply interfaced with a data acquisition card (PCI-6040E; National Instruments). Output power was regulated using a customized LabVIEW software. The UV light was delivered through the back port of an inverted microscope (IX 71; Olympus) equipped with a 10× objective, a 530LP dichroic mirror (T525 LPXR; Chroma), and a band-pass emission filter (BrightLine 562/40; Semrock). An EMCCD camera (iXon EM + DU-897; Andor Technology) was used to collect fluorescent images. Sequential imaging protocols were used to separate cADDis fluorescence from background fluorescence arising from the released cage into sequential camera frames [see Fig. S1(b) [33]].

F. Data analysis of cADDis fluorescence

The total cAMP concentration released at any time t can be expressed as

$$[\mathrm{cAMP}]_\mathrm{T} = c_i(t) = \int s_v(t)\mathrm{d}t = \int k_\mathrm{rel} I(t)\mathrm{d}t, \tag{13}$$

where $s_v(t)$ represents the virtual stimulus function, k_rel the photorelease rate, and $I(t)$ the light intensity. The cADDis time traces were analyzed by fitting the data with a modified binding isotherm using Origin (OriginLab):

$$\frac{[\mathrm{cAMP}\times\mathrm{cADDis}]}{[\mathrm{cADDis}]_\mathrm{T}} = \frac{[\mathrm{cAMP}]}{K_\mathrm{D}+[\mathrm{cAMP}]}, \tag{14}$$

where $[\mathrm{cADDis}]_\mathrm{T}$ is the total cADDis concentration, [cAMP] is the free cAMP concentration, and [cAMP·cADDis] is the concentration of the cAMP-cADDis complex. Assuming that the fluorescence signal is proportional to the complex concentration, then the change in cADDis fluorescence is given by

$$\frac{\Delta F(t)}{F} = A\frac{[\mathrm{cAMP}]}{K_\mathrm{D}+[\mathrm{cAMP}]}, \tag{15}$$

where A is a proportionality factor. When only a small fraction of the released cAMP binds to cADDis, the free and total cAMP concentrations are approximately equal. In this regime Eqs. (13) and (14), governing cAMP release and sensor binding, can be combined to yield a single expression describing the fluorescence trace as a function of the stimulus and experimental parameters:

$$\frac{\Delta F(t)}{F} \approx A\frac{\int s_v(t)\mathrm{d}t}{K_\mathrm{D}+\int s_v(t)\mathrm{d}t}. \tag{16}$$

The cADDis fluorescence time course was fitted to the above equation across various stimulus protocols: $s_v(t) = s_1$, $s_v(t) = s_2 t$, and $s_v(t) = s_2\sin(\omega t) + s_1$, corresponding to a step (constant), a ramp (linear increase), and a sinusoidal waveform, respectively.

G. Single-cell recordings using temporal light waveforms

Sperm loaded with DEACM-caged cGMP (15 μM) were diluted $1:10^6$ in ASW containing 0.5% Pluronic F127 (Sigma-Aldrich) and imaged in a custom-made observation chamber of 100-μM depth. Cyclic GMP was released by a 365 nm UV LED (M365L2; Thorlabs) with a custom-made power supply regulated via a data acquisition card (PCI-6040E; National Instruments). The output power was adjusted in time using a customized LabVIEW program. The UV power was calibrated using a photodiode (DET36A/m; Thorlabs). The UV light entered through the back port of an inverted microscope (IX 71; Olympus) equipped with a 10× objective (UPLSAPO10X; Olympus) and with a 495LP dichroic mirror (BS495 LP; Semrock). UV light was attenuated using a 2% neutral-density filter (Linos, Qioptiq Photonics) and filtered for imaging by a 510 LP emission filter (ET510LP; Chroma). The maximal light power delivered onto the sample (20 μW) was measured with a power meter (Fieldmax top and PowerMax PS19Q; Coherent). Dark-field illumination was achieved with a 730-nm LED (M730L4; Thorlabs) and a short working distance condenser (IX2-U-UCD8; Olympus). Dark-field images were recorded by an EMCCD camera (iXon EM+ DU-897; Andor Technology).

H. Analysis of single cells

Tracking of sperm cells from dark-field video microscopy data was done using a customized program written in MATLAB. The raw trajectory was smoothed to filter the fast head wiggling around the path centerline by a common local regression algorithm "lowess" with a span window of 200–250 ms or using the powersmooth algorithm [69] before further analysis. The swimming path curvature was calculated by a robust circle-fitting algorithm [70]. The sign of the curvature is defined as positive when the cell has a counterclockwise rotation. To calculate the frequency and phase of the oscillating signals, we began by applying the powersmooth method with a smoothing order of two to determine the baseline of the curve. Next, the "pure" oscillatory component was extracted by subtracting this baseline from the original signal. Finally, we performed sine-curve fitting on the isolated oscillatory component to compute its frequency and phase.

I. Transfer function calculation

The frequency sweep input was generated using the MATLAB chirp function, with an instantaneous frequency sweep given by

$$f(t) = f_0 + \beta t, \tag{17}$$

where $\beta = \frac{f_1 - f_0}{t_1}$, with f_0 is the instantaneous frequency at time 0, and f_1 is the instantaneous frequency at time t_1.

Multiple chirp $s_v(t)$ inputs were used sequentially on sperm from the same animal to cover a range between 0 and 15 Hz with an overlap in the frequency ranges of the inputs. The multiple inputs produced multiple outputs that were later used

to extract a set of impulse responses using the convolution theorem:

$$y_{\text{out}}(t) = \int_{-\infty}^{\infty} s_v(\tau) h(t-\tau) d\tau, \tag{18}$$

where y_{out} represents the measured Ca^{2+} output, s_v represents the virtual stimulus, and h the transfer function. The convolution theorem states that the Fourier transform of a convolution of two signals is the pointwise product of their Fourier transforms. Therefore, Eq. (18) can be written as

$$Y(f) = S(f) \cdot \mathbf{H}(f), \tag{19}$$

where Y is the Fourier transform of y_{out}, S is the Fourier transform of s_v, $\mathbf{H}$ is the Fourier transform of h, and f is the frequency. The magnitude and phase of the transfer function $\mathbf{H}$ were calculated as follows:

$$\begin{aligned} \text{Magnitude:} |\mathbf{H}(f)| &= \left| \frac{Y(f)}{S(f)} \right| \\ \text{Phase:} \angle \mathbf{H}(f) &= \angle Y(f) - \angle S(f), \end{aligned} \tag{20}$$

where $\angle \mathbf{H}(f)$, $\angle Y(f)$, and $\angle S(f)$ are the frequency-dependent phases of the transfer function, the output, and the input, respectively. The magnitude of the transfer function can be converted into the dB scale by $\mathbf{H}_{\text{dB}}(f) = 20\log_{10}|\mathbf{H}(f)|$. Finally, the set of transfer functions from the multiple chirps was averaged.

The transfer function was tested by providing a sinusoidal stimulus input carrying two frequencies (1 and 6 Hz), and the Ca^{2+} output was predicted as follows:

$$y_{Ca^{2+}} = F^{-1}\{Y_{Ca^{2+}}(f)\} = F^{-1}\{[S_{1\,\text{Hz}}(f) + S_{6\,\text{Hz}}(f)] \cdot \mathbf{H}(f)\}, \tag{21}$$

where F^{-1} is the inverse Fourier transform. The predicted output was in agreement with the measured Ca^{2+} signal [Fig. 4(d)]. All calculations were done using MATLAB single processing toolbox in a custom-made GUI. Data were post-processed and plotted using OriginLab.

J. Path simulation

All theoretical trajectories were calculated numerically using eqn. S4 and by time integration of the geometric definition of curvature [Eq. (S6); see also Note 3 [33]] with parameters $\kappa_0 = 12\,\text{mm}^{-1}$, $\beta = 0.04\,\text{s mm}^{-1}$ [40], $f_s = 1$ Hz, and $A_2 = 40$.

K. Remote control of single cells

The UV light gradient was generated by a Digital Light Processing (DLP) beamer with a 385 nm wavelength (Pro4500; Wintech Digital) collimated by one eyepiece lens (W10×/23; Carl Zeiss) and focused into the focal plane of the sample by a plano-convex lens (ACA254-150-A $f = 150$ mm; Thorlabs). A 425LP dichroic (425DCXR; Chroma) under the objective lens (UPLSAPO10X; Olympus) was used to couple the UV light onto the infinity-corrected light path of the microscope (IX 71; Olympus). A thin sample solution of sodium fluorescein (200 μM; Fluka Analytical) was imaged to estimate the shape of the UV gradient after passing all the optical components. Fluorescence emission was filtered by a 535/30 filter (ET535/30M; Chroma) and used to calculate a height-width ratio deformation factor, which was applied to all images projected by the DLP beamer. For loading, dry sperm were diluted 18:100 (v/v) in ASW containing 2.5 mM sodium Probenecid (AAT Bioquest), 0.5% Pluronic F127, and 30 μM [6,7-bis(ethoxycarbonylmethoxy)-coumarin-4-yl]methyl-cGMP (BECMCM-caged cGMP; [28,71]), and kept in the dark at 20 °C for 1 h. After loading, sperm were studied at $1:10^5$ dilution in ASW containing 30 μM BECMCM-caged cGMP, 2.5 mM Probenecid, and 0.5% Pluronic in a custom-made observation chamber with a 150-μM depth. Dark-field images were generated with a 660 nm LED light source (M660L3-C1; Thorlabs) and recorded (100 fps) by a fast monochrome camera (Dimax; PCO) after UV-light filtering by a 675/67 filter (FF02-675/67-25; Semrock). To increase the resolution of the Minerva shape formed by sperm, the Minerva stimulus was split into four parts, and the recorded videos were later connected.

ACKNOWLEDGMENTS

We thank Heike Krause for preparing the manuscript. Financial support by the Deutsche Forschungsgemeinschaft (DFG) via the priority program SPP 1726 "Microswimmers" (U.B.K., L.A., and B.M.F.) and the grants [313904155/SA1785/7–1, 380524518/SA1785/9–1, 214362475/GRK1873/2] (P.S.) are gratefully acknowledged. B.M.F. was supported by the German National Science Foundation (DFG) through the Excellence Initiative by the German Federal and State Governments (Clusters of Excellence cfaed EXC-1056 and "Physics of Life" (PoL) EXC-2068-390729961) and through a Heisenberg grant (421143374). A.M. was supported by a grant from the Italian Ministry of Education, University, and Research 2010599KRB. We thank Marco Gigante (SISSA Mechatronics Lab) for technical assistance in olfactory neuron experiments.

L.A., H.H., U.B.K., and R.S. designed the project; H.H., M.B., D.F., U.B.K., A.R., and R.S. performed the stopped-flow experiments; A.R. synthesized the caged compounds; L.A., A.G., F.L., and R.P. performed the motility experiments; H.H, A.G., L.A., and B.M.F analyzed data; L.A., B.M.F., and A.G. developed the theory for sperm motility; A.H.C., A.M., and S.P. designed and performed the electrophysiological experiments on olfactory neurons; V.D., B.K.F., and P.S. designed and performed the experiments on cardiac myocytes; H.H. and H.G.K. designed and performed the experiments on CHO cells; L.A., B.M.F., H.H., and U.B.K. wrote the manuscript; all authors edited and revised the manuscript.

The authors declare no competing financial interests.

DATA AVAILABILITY

The data that support the findings of this article are openly available [86].

[1] J. R. Taylor and R. Stocker, Trade-offs of chemotactic foraging in turbulent water, Science **338**, 675 (2012).

[2] A. Sengupta, F. Carrara, and R. Stocker, Phytoplankton can actively diversify their migration strategy in response to turbulent cues, Nature (London) **543**, 555 (2017).

[3] M. Lungarella and O. Sporns, Mapping information flow in sensorimotor networks, PLoS Comput. Biol. **2**, e144 (2006).

[4] S. J. Huston, M. Stopfer, S. Cassenaer, Z. N. Aldworth, and G. Laurent, Neural encoding of odors during active sampling and in turbulent plumes, Neuron **88**, 403 (2015).

[5] C. J. Brokaw, Chemotaxis of bracken spermatozoids, Ph.D. thesis, Cambridge University, 1958.

[6] T. Fenchel and N. Blackburn, Motile chemosensory behaviour of phagotrophic protists: Mechanisms for and efficiency in congregating at food patches, Protist **150**, 325 (1999).

[7] H. C. Crenshaw, A new look at locomotion in microorganisms: Rotating and translating, Amer. Zool. **36**, 608 (1996).

[8] R. Thar and T. Fenchel, True chemotaxis in oxygen gradients of the sulfur-oxidizing bacterium *Thiovulum majus*, Appl. Environ. Microb. **67**, 3299 (2001).

[9] M. McHenry and J. A. Strother, The kinematics of phototaxis in larvae of the ascidian *Aplidium constellatum*, Mar. Biol. **142**, 173 (2003).

[10] L. Clement, S. Schwarz, and A. Wystrach, An intrinsic oscillator underlies visual navigation in ants, Curr. Biol. **33**, 411, (2023).

[11] A. Gomez-Marin, G. J. Stephens, and M. Louis, Active sampling and decision making in *Drosophila* chemotaxis, Nat. Commun. **2**, 441 (2011).

[12] G. Jekely, J. Colombelli, H. Hausen, K. Guy, E. Stelzer, F. Nedelec, and D. Arendt, Mechanism of phototaxis in marine zooplankton, Nature (London) **456**, 395 (2008).

[13] M. Polin, I. Tuval, K. Drescher, J. P. Gollub, and R. E. Goldstein, Chlamydomonas swims with two "gears" in a eukaryotic version of run-and-tumble locomotion, Science **325**, 487 (2009).

[14] B. Mitchinson, R. A. Grant, K. Arkley, V. Rankov, I. Perkon, and T. J. Prescott, Active vibrissal sensing in rodents and marsupials, Philos. Trans. R. Soc. Lond. B Biol. Sci. **366**, 3037 (2011).

[15] D. Muzzey, C. A. Gomez-Uribe, J. T. Mettetal, and A. van Oudenaarden, A systems-level analysis of perfect adaptation in yeast osmoregulation, Cell **138**, 160 (2009).

[16] J. E. Toettcher, D. Gong, W. A. Lim, and O. D. Weiner, Light-based feedback for controlling intracellular signaling dynamics, Nat. Methods **8**, 837 (2011).

[17] T. S. Shimizu, Y. Tu, and H. C. Berg, A modular gradient-sensing network for chemotaxis in *Escherichia coli* revealed by responses to time-varying stimuli, Mol. Syst. Biol. **6**, 382 (2010).

[18] J. T. Mettetal, D. Muzzey, C. Gomez-Uribe, and A. van Oudenaarden, The frequency dependence of osmo-adaptation in *Saccharomyces cerevisiae*, Science **319**, 482 (2008).

[19] S. J. Rahi, J. Larsch, K. Pecani, A. Y. Katsov, N. Mansouri, K. Tsaneva-Atanasova, E. D. Sontag, and F. R. Cross, Oscillatory stimuli differentiate adapting circuit topologies, Nat. Methods **14**, 1010 (2017).

[20] S. Schröder-Lang, M. Schwärzel, R. Seifert, T. Strünker, S. Kateriya, J. Looser, M. Watanabe, U. B. Kaupp, P. Hegemann, and G. Nagel, Fast manipulation of cellular cAMP level by light *in vivo*, Nat. Methods **4**, 39 (2007).

[21] M. Stierl, P. Stumpf, D. Udwari, R. Gueta, R. Hagedorn, A. Losi, W. Gartner, L. Petereit, M. Efetova, M. Schwarzel, T. G. Oertner, G. Nagel, and P. Hegemann, Light modulation of cellular cAMP by a small bacterial photoactivated adenylyl cyclase, bPAC, of the soil bacterium *Beggiatoa*, J. Biol. Chem. **286**, 1181 (2011).

[22] V. Jansen, L. Alvarez, M. Balbach, T. Strünker, P. Hegemann, U. B. Kaupp, and D. Wachten, Controlling fertilization and cAMP signaling in sperm by optogenetics, eLife **4**, e05161 (2015).

[23] G. M. Avelar, R. I. Schumacher, P. A. Zaini, G. Leonard, T. A. Richards, and S. L. Gomes, A rhodopsin-guanylyl cyclase gene fusion functions in visual perception in a fungus, Curr. Biol. **24**, 1234 (2014).

[24] S. Gao, J. Nagpal, M. W. Schneider, V. Kozjak-Pavlovic, G. Nagel, and A. Gottschalk, Optogenetic manipulation of cGMP in cells and animals by the tightly light-regulated guanylyl-cyclase opsin CyclOp, Nat. Commun. **6**, 8046 (2015).

[25] U. Scheib, K. Stehfest, C. E. Gee, H. G. Korschen, R. Fudim, T. G. Oertner, and P. Hegemann, The rhodopsin-guanylyl cyclase of the aquatic fungus *Blastocladiella emersonii* enables fast optical control of cGMP signaling, Sci. Signal **8**, rs8 (2015).

[26] C. Gasser, S. Taiber, C. M. Yeh, C. H. Wittig, P. Hegemann, S. Ryu, F. Wunder, and A. Möglich, Engineering of a red-light-activated human cAMP/cGMP-specific phosphodiesterase, Proc. Natl. Acad. Sci. USA **111**, 8803 (2014).

[27] A. Hadjitheodorou, G. R. R. Bell, F. Ellett, S. Shastry, D. Irimia, S. R. Collins, and J. A. Theriot, Directional reorientation of migrating neutrophils is limited by suppression of receptor input signaling at the cell rear through myosin II activity, Nat. Commun. **12**, 6619 (2021).

[28] V. Hagen, S. Frings, J. Bendig, D. Lorenz, B. Wiesner, and U. B. Kaupp, Fluorescence spectroscopic quantification of the release of cyclic nucleotides from photocleavable [Bis(carboxymethoxy)coumarin-4-yl]methyl esters inside cells, Angew. Chem. Int. Ed. **41**, 3625 (2002).

[29] V. Hagen, K. Benndorf, U. B. Kaupp, C. M. Pavlos, H. Xu, J. P. Toscano, G. P. Hess, D. C. Gillespie, G. Kim, and K. Kandler, Control of cellular activity, in *Dynamic Studies in Biology*, edited by M. Goeldner and R. S. Givens (Wiley-VCH, Weinheim, 2005), Chap. 4, pp. 155–251.

[30] T. Eckhardt, V. Hagen, B. Schade, R. Schmidt, C. Schweitzer, and J. Bendig, Deactivation behavior and excited-state properties of (Coumarin-4-yl)methyl derivatives. 2. Photocleavage of selected (Coumarin-4-yl)methyl-caged adenosine cyclic 3′,5′-monophosphates with fluorescence enhancement, J. Org. Chem. **67**, 703 (2002).

[31] M. Kierzek, P. E. Deal, E. W. Miller, S. Mukherjee, D. Wachten, A. Baumann, U. B. Kaupp, T. Strünker, and C. Brenker, Simultaneous recording of multiple cellular signaling events by frequency- and spectrally-tuned multiplexing of fluorescent probes, eLife **10**, e63129 (2021).

[32] J. Y. Lin, A user's guide to channelrhodopsin variants: Features, limitations and future developments, Exp. Physiol. **96**, 19 (2011).

[33] See Supplemental Material at http://link.aps.org/supplemental/10.1103/hlkj-7yxd for additional details on experimental meth-

ods, notes, figures, tables, and movies, which includes Refs. [72–85].

[34] D. Wachten, J. F. Jikeli, and U. B. Kaupp, Sperm sensory signaling, Cold Spring Harb. Perspect. Biol. **9**, a028225 (2016).

[35] B. M. Friedrich and F. Jülicher, Chemotaxis of sperm cells, Proc. Natl. Acad. Sci. USA **104**, 13256 (2007).

[36] J. F. Jikeli, L. Alvarez, B. M. Friedrich, L. G. Wilson, R. Pascal, R. Colin, M. Pichlo, A. Rennhack, C. Brenker, and U. B. Kaupp, Sperm navigation along helical paths in 3D chemoattractant landscapes, Nat. Commun. **6**, 7985 (2015).

[37] B. M. Friedrich, I. H. Riedel-Kruse, J. Howard, and F. Jülicher, High-precision tracking of sperm swimming fine structure provides strong test of resistive force theory, J. Exp. Biol. **213**, 1226 (2010).

[38] A. Gong, S. Rode, U. B. Kaupp, G. Gompper, J. Elgeti, B. M. Friedrich, and L. Alvarez, The steering gaits of sperm, Philos. Trans. R. Soc. Lond. B Biol. Sci. **375**, 20190149 (2020).

[39] J. Elgeti, U. B. Kaupp, and G. Gompper, Hydrodynamics of sperm cells near surfaces, Biophys. J. **99**, 1018 (2010).

[40] L. Alvarez, L. Dai, B. M. Friedrich, N. D. Kashikar, I. Gregor, R. Pascal, and U. B. Kaupp, The rate of change in Ca^{2+} concentration controls sperm chemotaxis, J. Cell Biol. **196**, 653 (2012).

[41] U. B. Kaupp, J. Solzin, E. Hildebrand, J. E. Brown, A. Helbig, V. Hagen, M. Beyermann, F. Pampaloni, and I. Weyand, The signal flow and motor response controling chemotaxis of sea urchin sperm, Nat. Cell Biol. **5**, 109 (2003).

[42] H. Hamzeh, L. Alvarez, T. Strünker, M. Kierzek, C. Brenker, P. E. Deal, E. W. Miller, R. Seifert, and U. B. Kaupp, Kinetic and photonic techniques to study chemotactic signaling in sea urchin sperm, Methods Cell Biol. **151**, 487 (2019).

[43] R. Seifert, M. Flick, W. Bönigk, L. Alvarez, C. Trötschel, A. Poetsch, A. Müller, N. Goodwin, P. Pelzer, N. D. Kashikar, E. Kremmer, J. Jikeli, B. Timmermann, H. Kuhl, D. Fridman, F. Windler, U. B. Kaupp, and T. Strünker, The CatSper channel controls chemosensation in sea urchin sperm, EMBO J. **34**, 379 (2015).

[44] C. Trötschel, H. Hamzeh, L. Alvarez, R. Pascal, F. Lavryk, W. Bönigk, H. G. Körschen, A. Müller, A. Poetsch, A. Rennhack, L. Gui, D. Nicastro, T. Strünker, R. Seifert, and U. B. Kaupp, Absolute proteomic quantification reveals design principles of sperm flagellar chemosensation, EMBO J. **39**, e102723, (2020).

[45] N. D. Kashikar, L. Alvarez, R. Seifert, I. Gregor, O. Jäckle, M. Beyermann, E. Krause, and U. B. Kaupp, Temporal sampling, resetting, and adaptation orchestrate gradient sensing in sperm, J. Cell Biol. **198**, 1075 (2012).

[46] J. A. Kromer, S. Marcker, S. Lange, C. Baier, and B. M. Friedrich, Decision making improves sperm chemotaxis in the presence of noise, PLoS Comput. Biol. **14**, e1006109 (2018).

[47] M. Böhmer, Q. Van, I. Weyand, V. Hagen, M. Beyermann, M. Matsumoto, M. Hoshi, E. Hildebrand, and U. B. Kaupp, Ca^{2+} spikes in the flagellum control chemotactic behavior of sperm, EMBO J. **24**, 2741 (2005).

[48] M. Goeldner and R. Givens, *Dynamic Studies in Biology: Phototriggers, Photoswitches and Caged Biomolecules* (Wiley-VCH, 2005).

[49] W. Bönigk, A. Loogen, R. Seifert, N. Kashikar, C. Klemm, E. Krause, V. Hagen, E. Kremmer, T. Strünker, and U. B. Kaupp, An atypical CNG channel activated by a single cGMP molecule controls sperm chemotaxis, Sci. Signal **2**, ra68 (2009).

[50] R. Ma, G. S. Klindt, I. H. Riedel-Kruse, F. Jülicher, and B. M. Friedrich, Active phase and amplitude fluctuations of flagellar beating, Phys. Rev. Lett. **113**, 048101 (2014).

[51] I. Reiten, F. E. Uslu, S. Fore, R. Pelgrims, C. Ringers, C. Diaz Verdugo, M. Hoffman, P. Lal, K. Kawakami, K. Pekkan, E. Yaksi, and N. Jurisch-Yaksi, Motile-cilia-mediated flow improves sensitivity and temporal resolution of olfactory computations, Curr. Biol. **27**, 166 (2017).

[52] E. W. Olstad, C. Ringers, J. N. Hansen, A. Wens, C. Brandt, D. Wachten, E. Yaksi, and N. Jurisch-Yaksi, Ciliary beating compartmentalizes cerebrospinal fluid flow in the brain and regulates ventricular development, Curr. Biol. **29**, 229 (2019).

[53] M. Skoge, H. Yue, M. Erickstad, A. Bae, H. Levine, A. Groisman, W. F. Loomis, and W. J. Rappel, Cellular memory in eukaryotic chemotaxis, Proc. Natl. Acad. Sci. USA **111**, 14448 (2014).

[54] C. H. Huang and P. A. Iglesias, Cell memory and adaptation in chemotaxis, Proc. Natl. Acad. Sci. USA **111**, 15287 (2014).

[55] A. Nakajima, S. Ishihara, D. Imoto, and S. Sawai, Rectified directional sensing in long-range cell migration, Nat. Commun. **5**, 5367 (2014).

[56] D. B. Dusenbery, Spatial sensing of stimulus gradients can be superior to temporal sensing for free-swimming bacteria, Biophys. J. **74**, 2272 (1998).

[57] K. Y. Wan and G. Jekely, Origins of eukaryotic excitability, Philos. Trans. R. Soc. Lond. B Biol. Sci. **376**, 20190758 (2021).

[58] L. Alvarez, B. M. Friedrich, G. Gompper, and U. B. Kaupp, The computational sperm cell, Trends Cell Biol. **24**, 198 (2014).

[59] J. Rode, M. Novak, and B. M. Friedrich, Information theory of chemotactic agents using both spatial and temporal gradient sensing, PRX Life **2**, 023012 (2024).

[60] D. Cortese and K. Y. Wan, Control of helical navigation by three-dimensional flagellar beating, Phys. Rev. Lett. **126**, 088003 (2021).

[61] U. Rüffer and W. Nultsch, Flagellar photoresponses of *Chlamydomonas* cells held on micropipettes: II. Change in flagellar beat pattern, Cytoskeleton **18**, 269 (1991).

[62] R. R. Bennett and R. Golestanian, A steering mechanism for phototaxis in *Chlamydomonas*, J. R. Soc. Interface **12**, 20141164 (2015).

[63] https://github.com/Micro-Sandworms/Photolysis

[64] T. Strünker, I. Weyand, W. Bönigk, Q. Van, A. Loogen, J. E. Brown, N. Kashikar, V. Hagen, E. Krause, and U. B. Kaupp, A K^+-selective cGMP-gated ion channel controls chemosensation of sperm, Nat. Cell Biol. **8**, 1149 (2006).

[65] B. S. Moore, A. N. Stepanchick, P. H. Tewson, C. M. Hartle, J. Zhang, A. M. Quinn, T. E. Hughes, and T. Mirshahi, Cilia have high cAMP levels that are inhibited by Sonic Hedgehog-regulated calcium dynamics, Proc. Natl. Acad. Sci. USA **113**, 13069 (2016).

[66] J. de Rooij, H. Rehmann, M. van Triest, R. H. Cool, A. Wittinghofer, and J. L. Bos, Mechanism of regulation of the Epac family of cAMP-dependent RapGEFs, J. Biol. Chem. **275**, 20829 (2000).

[67] H. Rehmann, E. Arias-Palomo, M. A. Hadders, F. Schwede, O. Llorca, and J. L. Bos, Structure of Epac2 in complex with a cyclic AMP analogue and RAP1B, Nature (London) **455**, 124 (2008).

[68] S. Mukherjee, V. Jansen, J. F. Jikeli, H. Hamzeh, L. Alvarez, M. Dombrowski, M. Balbach, T. Strünker, R. Seifert, U. B. Kaupp, and D. Wachten, A novel biosensor to study cAMP dynamics in cilia and flagella, eLife **5**, e14052 (2016).

[69] B. M. Friedrich, powersmooth, MATLAB Central File Exchange (2025), https://www.mathworks.com/matlabcentral/fileexchange/48799-powersmooth.

[70] G. Taubin, Estimation of planar curves, surfaces, and nonplanar space curves defined by implicit equations with applications to edge and range image segmentation, IEEE Trans. Pattern Anal. Mach. Intell. **11**, 1115 (1991).

[71] V. Hagen, J. Bendig, S. Frings, T. Eckardt, S. Helm, D. Reuter, and U. B. Kaupp, Highly efficient and ultrafast phototriggers for cAMP and cGMP by using long-wavelength UV/Vis-activation, Angew. Chem. Int. Ed. **40**, 1046 (2001).

[72] E. G. Lakatta and D. DiFrancesco, What keeps us ticking: A funny current, a calcium clock, or both? J. Mol. Cell Cardiol. **47**, 157 (2009).

[73] T. Bruegmann, D. Malan, M. Hesse, T. Beiert, C. J. Fuegemann, B. K. Fleischmann, and P. Sasse, Optogenetic control of heart muscle *in vitro* and *in vivo*, Nat. Methods **7**, 897 (2010).

[74] D. DiFrancesco and P. Tortora, Direct activation of cardiac pacemaker channels by intracellular cyclic AMP, Nature (London) **351**, 145 (1991).

[75] A. Koschinski and M. Zaccolo, Activation of PKA in cell requires higher concentration of cAMP than *in vitro*: Implications for compartmentalization of cAMP signalling, Sci. Rep. **7**, 14090, (2017).

[76] B. Z. Jia, Y. Qi, J. D. Wong-Campos, S. G. Megason, and A. E. Cohen, A bioelectrical phase transition patterns the first vertebrate heartbeats, Nature (London) **622**, 149 (2023).

[77] M. Dibattista, S. Pifferi, A. Boccaccio, A. Menini, and J. Reisert, The long tale of the calcium activated Cl(−) channels in olfactory transduction, Channels (Austin) **11**, 399 (2017).

[78] G. Pietra, M. Dibattista, A. Menini, J. Reisert, and A. Boccaccio, The Ca^{2+}-activated Cl- channel TMEM16B regulates action potential firing and axonal targeting in olfactory sensory neurons, J. Gen. Physiol. **148**, 293 (2016).

[79] M. Wachowiak, All in a sniff: Olfaction as a model for active sensing, Neuron **71**, 962 (2011).

[80] A. S. Ghatpande and J. Reisert, Olfactory receptor neuron responses coding for rapid odour sampling, J. Physiol. **589**, 2261 (2011).

[81] K. D. Cygnar and H. Zhao, Phosphodiesterase 1C is dispensable for rapid response termination of olfactory sensory neurons, Nat. Neurosci. **12**, 454 (2009).

[82] Y. Song, K. D. Cygnar, B. Sagdullaev, M. Valley, S. Hirsh, A. Stephan, J. Reisert, and H. Zhao, Olfactory CNG channel desensitization by Ca^{2+}/CaM via the B1b subunit affects response termination but not sensitivity to recurring stimulation, Neuron **58**, 374 (2008).

[83] J. Reisert and H. Zhao, Perspectives on: Information and coding in mammalian sensory physiology: Response kinetics of olfactory receptor neurons and the implications in olfactory coding, J. Gen. Physiol. **138**, 303 (2011).

[84] A. B. Stephan, S. Tobochnik, M. Dibattista, C. M. Wall, J. Reisert, and H. Zhao, The Na^{+}/Ca^{2+} exchanger NCKX4 governs termination and adaptation of the mammalian olfactory response, Nat. Neurosci. **15**, 131 (2011).

[85] N. Chernov, Circle Fit (Taubin method), MATLAB Central File Exchange (2025), https://www.mathworks.com/matlabcentral/fileexchange/22678-circle-fit-taubin-method.

[86] https://edmond.mpg.de/dataset.xhtml?persistentId=doi:10.17617/3.6TFIWX